# UAV-Based Far-Field Antenna Pattern Measurement Method for Polarimetric Weather Radars: Simulation and Error Analysis

**ARTURO YOSHIYUKI UMEYAMA**[ID], **(Member, IEEE), JORGE L. SALAZAR-CERRENO**[ID],
**(Senior Member, IEEE), AND CALEB J. FULTON**[ID], **(Senior Member, IEEE)**

Advanced Radar Research Center, The University of Oklahoma, Norman, OK 73019, USA
School of Electrical and Computer Engineering, The University of Oklahoma, Norman, OK 73019, USA

Corresponding author: Jorge L. Salazar-cerreno (salazar@ou.edu)

**ABSTRACT** Continuing advances and the availability of relatively inexpensive commercial off-the-shelf UAV systems allow the development of in-situ antenna measurement systems for a wide variety of operating frequencies and applications. This paper presents a simulation framework and error analysis that provides a guideline for in-situ far-field (FF) unmanned aerial vehicle (UAV)-based antenna measurements of operational and research antennas for polarimetric weather radar systems. The analysis includes system design trade-offs which allow the evaluation of antenna measurement errors due to UAV position, gimbal orientation, and extraneous error sources that can be present in a UAV-based field-testing scenario. Results analyzed for all cases provide error bounds and limitations for two example characterization schemes. The UAV-based antenna measurement system simulation and analysis suggests and supports the feasibility of such a system for antenna characterization and polarimetric calibration of antennas in the near future.

**INDEX TERMS** Antenna characterization, errors, in-situ measurements, UAV, antenna test.

## I. INTRODUCTION

In the recent decade, the cross-agency program SENSR (Spectrum Efficient National Surveillance Radar) is planning to migrate the current dish-based and mechanically steered weather radar system (WSR-88D and NEXRAD [1]) into fully digital dual-polarized multifunction phased array weather radar systems with electronic scanning capabilities. These systems, which operate mostly in S band (2.8-3.2 GHz), require accurate characterization and calibration of their components to ensure that no biases are being introduced in the polarimetric weather radar products [2], [3]. Since the radiation properties in digital phased array antennas depend on the electronic scanning direction, additional challenges arise in their calibration. This imposes a strict requirement on the mismatch between the co-polarization patterns of no greater than 0.1 dB, and cross-polarization levels of no greater than about −50 dB, of the antenna

The associate editor coordinating the review of this manuscript and approving it for publication was Shah Nawaz Burokur[ID].

for simultaneous transmit and simultaneous receive (STSR) operation mode [4]. Therefore, an in-situ antenna measurement method that complies with such demands is necessary to calibrate each radar in the network.

To accurately characterize antennas, specialized indoor or outdoor antenna range facilities are required for testing and evaluating the antenna's radiation characteristics. They consist of the appropriate RF instrumentation, technical procedures, and physical space required for the measurements. The design and construction of such facilities can introduce additional space and cost constraints upon the antenna installation site, and, furthermore, an antenna characterized in an indoor facility will not necessarily perform identically in an outdoor environment under normal operating conditions [5]–[7]. In other words, the intrinsic radiation characteristics and the overall performance of an antenna may be substantially modified due to a number of factors of its working environment (e.g., temperature, humidity, weather conditions, ground clutter, RF interference, morphology, component failure rate, and others) [8]. An outdoor in-situ range can adequately measure

the antenna system's performance in its final installation site, to ensure that it meets the requirements, and that its interaction with the environment is predictable [5]–[7]. For example, elevated ranges are typically used to test physically large antennas where the antennas are mounted on elevated structures and/or terrains, and are generally designed to operate over a mostly flat area and to mitigate the effects of its surroundings by a number of design criteria, which include a careful selection of the probe antenna, its mounting structure and position, the terrain, and other structural elements to redirect or absorb reflected energy [5]–[7]. Unfortunately, it can easily become cost-prohibitive and impractical to develop such facilities for networks with a large number of radars.

To overcome this, a wide variety of methods and equipment for non-fixed in-situ antenna measurements have been employed in the past, which do not require large facilities around the antenna under test (AUT), including tethered balloons [9] and helicopters [10], [11]. These airborne methods [9]–[27] have been used in measuring the farfield (FF) radiation patterns of large antennas for a wide variety of applications and operating frequencies, offering improvements over cost constraints and allowing antenna test and evaluation solutions to be deployable for multiple sites. The measurements are performed using an antenna mounted on an airborne platform, which can range from manned aircraft [10], [11], up to small and micro unmanned aerial vehicles (UAV) [12]–[27]. In this context, a UAV-based antenna range could provide a cost-effective method for in-situ antenna characterization since it does not require extensive modification of the antenna test site and is generally portable from one site to the other. It is still unknown, however, how and to what extent environmental factors, flight strategies, and stability of the UAV may affect the measurements, especially in the case of polarimetric phased array weather radars (which typically operate in S band) which require a high degree of accuracy in the co- and crosspolarization antenna patterns. While [28] explores the calibration of a weather radar using a UAV and a metallic sphere, as of the time of this writing, no other work relates to the characterization *and* calibration of *polarimetric* weather radars, which includes a framework that allows a quick evaluation of the impact of potential error sources before performing in-situ measurements. A preliminary assessment of the field conditions can be performed beforehand to establish the best measurement configuration in terms of height, range, flight mode, wind conditions, and extraneous reflections mitigation by accounting for error sources in FF antenna measurements by following certain guidelines [5]. To adequately assess such potential effects prior to performing field tests, a mathematical framework that includes realistic models of the AUT, probe antenna, and environmental factors (e.g., undesired reflections, position and orientation disturbance) is convenient and shall be presented in this work.

A summary of the guidelines for FF measurements applied to UAV-based antenna measurements in terms of design, instrumentation, and procedure considerations are presented

in Section II. The simulation framework for the UAV-based measurement method presented herein, and its error modeling, are described in Section III, while analysis and results for a particular set of case studies is presented in Section IV. Finally, a brief discussion summarizing the findings of this work is presented in Section V.

## II. FAR FIELD GUIDELINES FOR UAV-BASED MEASUREMENTS

With recent advances in commercially-off-the-shelf available technology for UAVs, it has become far more cost-effective to develop improved UAV-based antenna measurement solutions [12]–[27]. The main advantage UAVs provide is that they are not restricted in movement, and with the use of a gimbal, it is possible to have an airborne measurement system with multiple degrees of freedom. However, it becomes critical to suppress reflections and signals from undesired sources, and to compensate for misalignment between the probe antenna and the AUT, since these factors rely on the position and orientation of the UAV and gimbal. Naturally, this adds uncertainties in the measurements because the platform is generally subject to unfavorable environmental conditions. The measurements also depend on the precision of the on-board instrumentation, as well as the flight/scan procedure selected. Recent works [29]–[34] have investigated the measurement of both magnitude and phase in near field (NF) to obtain the FF antenna pattern through NF-to-FF transformation for large aperture antennas using UAVs. However, this work is limited to testing the FF amplitude of the of the co-, and cross-polarization antenna radiation pattern. This section focuses on the most relevant antenna range design criteria, instrumentation, and procedures applicable to UAV-based FF pattern measurements for polarimetric weather radar antennas.

### A. GENERAL DESIGN CONSIDERATIONS
Much like in conventional outdoor FF antenna ranges, in UAV-based antenna measurements, the standard criteria [5], [6] must be adhered to, to ensure the measurement errors are minimal. From them, a set of criteria may be derived for UAV-based FF measurements by taking into account the mobility of the platform, and by not imposing any restriction on the type of probe antenna that can be used. Some of the effects that are considered herein for the design requirements are presented next.

### 1) EFFECT OF PHASE CURVATURE
While the illuminating field is assumed to be a uniform plane wave for FF purposes, in reality, the phase variation is closer to that of a spherical wave emanating from the phase center of the probe antenna (see Fig. 1). A variation in the phase of the illuminating field will occur if the receiving antenna subtends less than a half-power beamwidth of the transmitting antenna's wave front. This phase error will produce an error in the measured amplitude at boresight, and a significant effect on the side-lobe level (SLL) and shape of the antenna
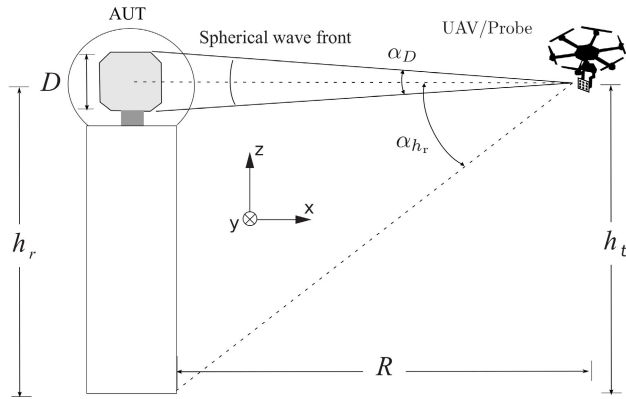
**FIGURE 1.** FF measurement configuration for the UAV, probe antenna, and AUT. The sketch depicts a spherical wave front leaving the probe antenna and impinging on the aperture of the AUT.

radiation pattern [6]. An expression for the FF distance can be derived as

$$R \geq \frac{KD^2}{\lambda}, \tag{1}$$

where $D$ is the aperture of the receiving antenna (or AUT), $\lambda$ is the operating wavelength, and $K$ is a constant related to the phase error. For example, for $K = 2$, which is typically accepted as the minimum FF distance, the error in measurement is approximately 0.1 dB [35]. For UAV-based measurements, this requirement can be easily met in virtue of the mobility of the UAV platform.

#### 2) EFFECT OF TRANSVERSAL AMPLITUDE TAPER
A taper in the amplitude of the excitation function across the aperture of the AUT can produce errors in the measured radiation pattern, manifested as a reduction of the directivity, and variations in the SLL; i.e., this effect is closely related to the beamwidth of the probe antenna [5]. For UAV-based measurements with an arbitrary probe antenna, this amplitude taper criterion may be derived as

$$\theta_\Delta \geq \alpha_D, \tag{2}$$

where $\theta_\Delta$ is the beamwidth of the probe antenna at the desired level $\Delta$ of maximum amplitude taper, and $\alpha_D$ is the angle subtended at the probe antenna by the AUT aperture width $D$ (Fig. 1), which is geometrically defined as

$$\alpha_D = 2\tan^{-1}\left(\frac{D}{2R}\right). \tag{3}$$

Equations (2) and (3) establish a relationship between the probe antenna beamwidth, the AUT aperture width, and the range at which the measurement is being performed. As a rule of thumb, an amplitude taper of 0.25 dB at the edges of the aperture (i.e., a 0.25-dB beamwidth, or $\theta_{0.25}$), yields errors in directivity no larger than 0.1 dB [6].

#### 3) EFFECT OF GROUND REFLECTIONS
A basic design goal is to have the range surface in front of the AUT not intercept any energy contained in the main lobe of the antenna probe [5]. To achieve this in UAV-based measurements, the first null in the probe antenna radiation pattern should be directed toward the base of the AUT tower (Fig. 1). This is equivalent to establishing that the plane angle subtended at the probe antenna by the AUT height and its phase center be equal to half of the first null beamwidth (FNBW) of the probe antenna (assuming a symmetrical radiation pattern), that is:

$$\frac{\text{FNBW}}{2} \leq \alpha_{h_r}, \tag{4}$$

$$\alpha_{h_r} = \tan^{-1}\left(\frac{h_r}{R}\right), \tag{5}$$

where $h_r$ is the height of the AUT. Strategies to mitigate the effect of the reflections from the range surface (e.g., diffraction fences, longitudinal ramps) are not included in this work, since they require modifications of the test site and incur in additional costs.

#### 4) SUMMARY
Table 1 summarizes the most important aspects to consider in the design and mitigation of errors for UAV-based measurements. Ideally, all three criteria should be met simultaneously, meaning that there will be restrictions on $R$ for the UAV platform, and $\theta_\Delta$ and FNBW for the probe antenna, depending on the tolerable measurement error levels $\Delta$, and the aperture $D$ and height $h_r$ of the AUT. It should be noted that these criteria for UAV-based measurements are only intended to be used as a guideline for selecting a suitable geographical location and probe antenna, and that they may not be simultaneously met at all times depending on the flight or scanning strategies. In such cases, a careful assessment would provide better insight of the error bounds.

**TABLE 1.** Summary of design considerations for UAV-base antenna measurements.

| Parameter | Generalized criterion |
|---|---|
| Phase curvature | $R \geq \frac{KD^2}{\lambda}$ |
| Transversal taper | $\theta_\Delta \geq \alpha_D$ |
| Ground reflections | $\frac{\text{FNBW}}{2} \leq \alpha_{h_r}$ |

### B. RF INSTRUMENTATION
The extent of the required instrumentation depends upon the functional requirements imposed by the measurements to be made. An antenna range is typically classified into five subsystems [7]: *transmitting subsystem* (including *probe antenna*), *receiving subsystem*, *positioning subsystem*, *recording subsystem*, and *data-processing subsystem*. Such a classification will be adopted here since, in general, one or more of these subsystems may be present in the

ground hardware, the flight hardware, or both. Additionally, because the mechanical airborne and ground instrumentation may vary widely in performance and noting that the accuracy and precision requirements would depend on the application, it is out of the scope of this work to present a discussion on each specific hardware. However, the basic RF instrumentation that allows FF magnitude measurements for co- and cross-polarization antenna patterns, for polarimetric weather radars, is discussed herein.

### 1) TRANSMITTING AND RECEIVING SUBSYSTEMS

The UAV can be operating as the transmitter or receiver as long as the required equipment is installed. In either case, the payload and size constraints are the main limitations of the UAV that one must account for. The transmitting subsystem includes the probe antenna, signal source, and the signal source control, and it must be selected so that it has frequency control, frequency stability, spectral purity, required power level, and modulation. For antenna amplitude measurements, it is important that the output of the signal source remain relatively constant [5]. The receiving system will include an oscilloscope or spectrum analyzer, and the corresponding back end chain of components needed to capture the transmitted signals at an adequate sensitivity, frequency, bandwidth, and dynamic range.[1]

The antenna to be mounted on the UAV must be selected such that the gain, beamwidth, band of operation, and polarization is appropriate for the specific measurement requirement and the general design considerations listed in Table 1. As far as the power level is concerned, the required power output of the signal source for a particular measurement is dependent upon the probe antenna and AUT gains, the receiver sensitivity, the transmission loss between the two antennas, and the dynamic range required for the measurement. Regardless of whether it is operating as a transmitter or receiver, the endurance of the UAV should be such that it permits the safe operation of the aircraft and on-board equipment for as long as the measurement procedure lasts. An additional factor to consider is the operation of such instruments under different environmental conditions; as such, it is a good practice to have weather-resistant equipment or to weather-proof the UAV frame.

### 2) POSITIONING, RECORDING, AND DATA-PROCESSING SUBSYSTEMS

The positioning subsystem will consist of the UAV platform and any instrument related to position tracking and orientation adjustment of the antenna, e.g., global positioning system (GPS), inertial measurement unit (IMU), barometer, gimbal, and the link to the ground base station. Alternatively, tracking devices external to the UAV platform may be used; e.g., laser trackers, computer vision, or differential GPS (DGPS). The accuracy of each component should be taken into account

---

[1]A dynamic range of at least 60 dB would be necessary to accurately measure the cross-polarization pattern in weather radar systems.

when assessing the potential alignment error sources in the measurements. To achieve the principal plane cuts, accurate positioning of the UAV and proper flight strategy are required, which cover the full range of two orthogonal axes $(\theta, \phi)$ depending on the operational mode of the AUT or radar system (e.g., mechanical or electronic scanning). It is desired that the operational coordinate system of the UAV matches that of the AUT to prevent misinterpretation of measured data and error evaluation.

As for the recording subsystem, a means to synchronize the ground station and UAV georeferencing data must be accounted for. A simple way to achieve this is by logging the position, orientation, and timestamp for each measurement taken, which is usually done automatically in the flight controller logs. Alternatively, this option may be provided by a DGPS with real-time kinematics (RTK), which further improves the position accuracy and precision.

### C. PROCEDURES

Field probing by continuous movement of the UAV allows rapid and systematic experimental evaluation of those parameters which affect the level of energy coming to the AUT. In general, a distant probe is carried by an airborne vehicle, which is maneuvered through the space surrounding the AUT to produce essentially plane waves illuminating the AUT from all directions of interest, and when the position and/or orientation of the antenna probe relative to the AUT changes, a variation in the received signal occurs. The direction to the probe with respect to a reference direction at the AUT is obtained from a tracking device which logs the position and orientation data in real time, or at post-processing. The error introduced because of the misalignment (position and orientation) between the AUT and the tracking device must be taken into account. Additionally, it may be necessary to determine the range to the probe to compute the correction, or to correct for the change in the incident power flux density caused when the aircraft does not fly perfectly along its intended route about the AUT. The amplitude of the signal received by the antenna provides the amplitude data to the recording device which is then processed to display the measurements as desired [5]. The probe must be in the FF region of the AUT, and if not possible, near- to far-field (NF-to-FF) transformation techniques and instrumentation must be used properly [29]–[34].

The process of pattern measurement and recording may involve either a point-by-point or a continuous method. Various scanning strategies have been implemented for UAV-based measurements [8], [24], [36]. These include: *hovering*, *planar (horizontal or vertical)*, *cylindrical*, and *spherical (azimuth or elevation)*. The hovering strategy is identical, in principle, to an elevated range, with the exception that the probe antenna is now mobile, with the UAV hovering in place while the AUT is rotating. Planar scans are the simplest to implement as rectilinear flight paths in the flight controller, and can be horizontal, e.g., flying above the AUT, or vertical, e.g., a plane normal to the direction of propagation.

Cylindrical scans consist of equiradial concentric circular patterns centered at the AUT with different heights. Spherical scans consist of concentric circles around the AUT either in horizontal planes or in vertical planes. A study of the time taken and the area covered for different systems is presented as examples in [8]. Additionally, the endurance of the UAV and the length in time of the scan must be taken into consideration with regards to the measurement characteristics that are desired.

To verify the alignment between the antennas, the UAV can be operated and data gathered continuously along, and across radials, and for different altitudes around a certain region of interest to establish the relative levels of the major contributors of extraneous signals distorting the incident field and the angles of the sources from the line of sight. The probe antenna should be oriented so that the peak of the main beam is in the direction of the AUT, and the pattern should be sufficiently uniform to avoid excessive amplitude tapering across the test aperture. Careful selection of the probe antenna can further reduce the effects of extraneous reflections due to the aircraft structure and asymmetry. Additionally, to determine the polarization characteristics of the illuminating field at the AUT it is also necessary that the roll axis of the probe antenna be adjustable or that the antenna be dual-polarized. The latter is preferred since measurements for both polarizations can be obtained during a single test operation and is analogous to the STSR operation in weather radars.

## III. SIMULATION FRAMEWORK

A simulation framework is developed which will be used in studying the feasibility of UAV-based FF measurements for weather radars, and to estimate the error levels to be expected in field experiments. This framework takes into account the design criteria presented in the previous section, as well as sources of error, and ideal models for the AUT and probe antenna (which can be replaced by any arbitrary model). This tool is important in establishing optimal scanning strategies and correction techniques when performing antenna measurements with UAVs. Additionally, the framework developed in this context shall be used to evaluate error sources in different outdoor antenna measurement configurations.

### A. ANTENNA AND TRANSMISSION MODELS

#### 1) AUT AND PROBE ANTENNAS

The general equations used for the complex electric field and antenna models, for planar phased array antennas, are [37], [38]:

$$E(\theta, \phi) = \frac{E_0}{r} f(\theta, \phi) \mathrm{AF}(\theta, \phi) e^{-jkr}, \tag{6}$$

$$\begin{aligned} \mathrm{AF}(\theta, \phi) = \frac{1}{N_x N_y} \sum_m \sum_n |a_{mn}| \exp\{-jk \\ \times [d_m(\sin\theta\cos\phi - \sin\theta_0\cos\phi_0) \\ + d_n(\sin\phi - \sin\phi_0)]\}, \end{aligned} \tag{7}$$

$$f(\theta, \phi) = \begin{bmatrix} f_{HH}(\theta, \phi) & f_{VH}(\theta, \phi) \\ f_{HV}(\theta, \phi) & f_{VV}(\theta, \phi) \end{bmatrix}, \tag{8}$$

$$f_{HH}(\theta, \phi) = [\cos(\theta)\cos(\phi)]^{n_{HH}}, \tag{9}$$

$$f_{VH}(\theta, \phi) = A_{VH}[\sin(\theta)\sin(\phi)]^{n_{VH}}, \tag{10}$$

$$f_{VV}(\theta, \phi) = [\cos(\theta)\cos(\phi)]^{n_{VV}}, \tag{11}$$

$$f_{HV}(\theta, \phi) = A_{HV}[\sin(\theta)\sin(\phi)]^{n_{HV}}, \tag{12}$$

where $E_0$ is a constant which depends on the antenna characteristics, $r$ is the range from the antenna, $k$ is the wave number which is related to the operating wavelength $\lambda$ by $k = 2\pi/\lambda$, AF is the antenna array factor for $\theta$ in azimuth and $\phi$ in elevation, with $\theta_0$ and $\phi_0$ the steered beam direction, $a_{mn}$ is the excitation function of the array, and $d_{m,n}$ is the offset of the element at the $m$-th and $n$-th positions, respectively. In addition, the element factor or antenna pattern $f$ is a matrix defined by the co-polarized and cross-polarized antenna patterns in the horizontal or vertical polarizations denoted by: $f_{HH}$ or H-transmit/H-receive, $f_{VH}$ or V-transmit/H-receive, $f_{VV}$ or V-transmit/V-receive, and $f_{HV}$ or H-transmit/V-receive. The coefficients are selected to match typical ideal antenna pattern characteristics, where the co-polarized patterns are assumed to have a cosine variation with a coefficient $n_{HH} = n_{VV} = 1.2$, and the cross-polarized patterns are assumed to have a sine form with $n_{VH} = n_{HV} = 0.4$. The AUT is assumed, though it can be generalized, to be similar to a phased array antenna operating at a frequency of 3 GHz ($\lambda = 10$ cm), which consists of $N_x = N_y = 80$ elements, an aperture size of $D_x = D_y = 4$ m, and an element spacing of $d = \lambda/2$. The AUT excitation function is assumed to be a uniform distribution across all elements of the array, although this may be slightly modified due to amplitude tapering effects (discussed in Section II-A), which depend on the angle $\alpha_D$ from (3) subtended by the AUT aperture at the probe. With said configuration, the beamwidth is equal to 1.26°, with a SLL of −13.25 dB and a maximum cross-polarization level of approximately −30 dB at $\theta = \phi = 45°$. The probe antenna uses an equivalent model as the one described for the AUT model, with a different number of elements and aperture of the array, corresponding to a 4 × 4 probe ($N_x = N_y = 4$) with an aperture of $d_x = d_y = 20$ cm, a beamwidth of 26.3°, a SLL of −11.4 dB, and a FNBW of 60°. The parameters selected here reflect those of the test bed that is part of this project [27], [39].

#### 2) TRANSMISSION MODEL

Using Friis' transmission equation [40], the amplitude of the transmitted signal can be estimated, and knowing that $P \propto E^2$ –that is, the power delivered is proportional to the square-power of the voltage– and that the antenna directivity is related to is amplitude pattern, an expression for the signal can be obtained as

$$E_D(\theta, \phi) = \frac{E_0}{r_D} f^{AUT}(\theta, \phi) f^P(\theta, \phi) e^{-jkr_D}, \tag{13}$$

where the subscript D indicates direct-path ray. The probe and AUT antenna patterns are represented by

$$f^P(\theta, \phi) = \begin{bmatrix} f_{HH}^P(\theta, \phi) & f_{VH}^P(\theta, \phi) \\ f_{HV}^P(\theta, \phi) & f_{VV}^P(\theta, \phi) \end{bmatrix} \mathrm{AF}^P(\theta, \phi), \tag{14}$$

$$f^{\mathrm{AUT}}(\theta, \phi) = \begin{bmatrix} f_{\mathrm{HH}}^{\mathrm{AUT}}(\theta, \phi) & f_{\mathrm{VH}}^{\mathrm{AUT}}(\theta, \phi) \\ f_{\mathrm{HV}}^{\mathrm{AUT}}(\theta, \phi) & f_{\mathrm{VV}}^{\mathrm{AUT}}(\theta, \phi) \end{bmatrix} \mathrm{AF}^{\mathrm{AUT}}(\theta, \phi). \tag{15}$$

By combining (13)-(15) and performing the matrix multiplication, the co-polarized and cross-polarized components of the measured signal may be obtained as:

$$E_{\mathrm{D,HH}} = \frac{E_0}{r_{\mathrm{D}}} \left( f_{\mathrm{HH}}^{\mathrm{AUT}} f_{\mathrm{HH}}^{\mathrm{P}} + f_{\mathrm{VH}}^{\mathrm{AUT}} f_{\mathrm{HV}}^{\mathrm{P}} \right) e^{-jkr_{\mathrm{D}}}, \tag{16}$$

$$E_{\mathrm{D,VH}} = \frac{E_0}{r_{\mathrm{D}}} \left( f_{\mathrm{HH}}^{\mathrm{AUT}} f_{\mathrm{VH}}^{\mathrm{P}} + f_{\mathrm{VH}}^{\mathrm{AUT}} f_{\mathrm{VV}}^{\mathrm{P}} \right) e^{-jkr_{\mathrm{D}}}, \tag{17}$$

$$E_{\mathrm{D,VV}} = \frac{E_0}{r_{\mathrm{D}}} \left( f_{\mathrm{VV}}^{\mathrm{AUT}} f_{\mathrm{VV}}^{\mathrm{P}} + f_{\mathrm{HV}}^{\mathrm{AUT}} f_{\mathrm{VH}}^{\mathrm{P}} \right) e^{-jkr_{\mathrm{D}}}, \tag{18}$$

$$E_{\mathrm{D,HV}} = \frac{E_0}{r_{\mathrm{D}}} \left( f_{\mathrm{HV}}^{\mathrm{AUT}} f_{\mathrm{HH}}^{\mathrm{P}} + f_{\mathrm{VV}}^{\mathrm{AUT}} f_{\mathrm{HV}}^{\mathrm{P}} \right) e^{-jkr_{\mathrm{D}}}, \tag{19}$$

where the $\theta$ and $\phi$ dependency has been omitted for simplicity.

## B. UAV STRUCTURE INFLUENCE

The signal of the probe antenna is slightly modified when it is mounted on the UAV, due to interactions (e.g., coupling and reflections) with the structure of the UAV. A few studies [41]–[45] have analyzed the interaction of the UAV structure and its EM radiation properties in free space with a probe antenna; however, a way to predict such effects at S band for weather radar antenna measurement purposes has not yet been investigated. Since a model of such phenomenon would be extremely difficult to accurately derive analytically, a simple radiating element model is chosen as

$$f_{\mathrm{R,UAV}}^{i} = f^{\mathrm{P}}(\theta_{\mathrm{R}}^{i}, \phi_{\mathrm{R}}^{i}) \frac{e^{-jkr_{\mathrm{R}}^{i}}}{r_{\mathrm{R}}^{i}} \left( A + B\cos(C\theta)\cos(C\phi) \right), \tag{20}$$

where $f^{\mathrm{P}}(\theta_{\mathrm{R}}^{i}, \phi_{\mathrm{R}}^{i})$ is the value of the probe antenna pattern for the $i$-th radiating element in the incidence direction relative to the phase center of the probe antenna, $r_{\mathrm{R}}^{i}$ is the distance to the $i$-th radiating element, and a ripple and roll-off model is dictated by the constants $A$, $B$, and $C$. Such constants are determined ad hoc to match measurements and simulations previously done for similar antennas in a controlled environment [26], [27]. The probe-only patterns, and the modified patterns with the UAV structure effects and geometries are presented in Fig. 2b.

The hexacopter model is selected for this study, with $L_g = 15$ cm, $Z_g = 30$ cm, $L_{\mathrm{arm}} = 35$ cm, the angle between the arms 60°, and two radiating elements placed at the extremes of the front-facing arms with the model described by (20) (see Fig. 2a). With this geometry, and the values of $A = 0.05$, $B = 0.15$, and $C = 30$, a ripple of approximately $\pm 0.16$ dB is obtained in the co-polarization pattern, with a cross-polarization level below $-40$ dB. This effect is added linearly to the radiation pattern of the probe. By simulating an ideal probe antenna, the cross-polarization levels for the probe alone are very small, and hence, not noticeable in the plots.
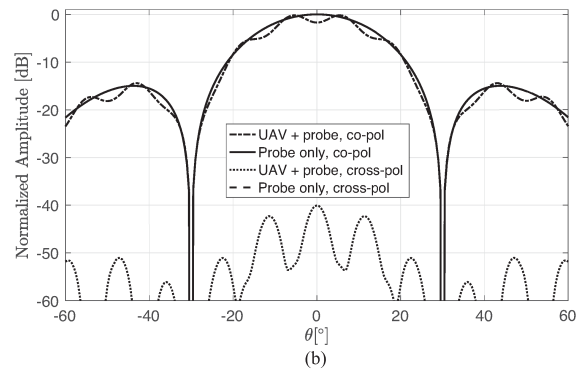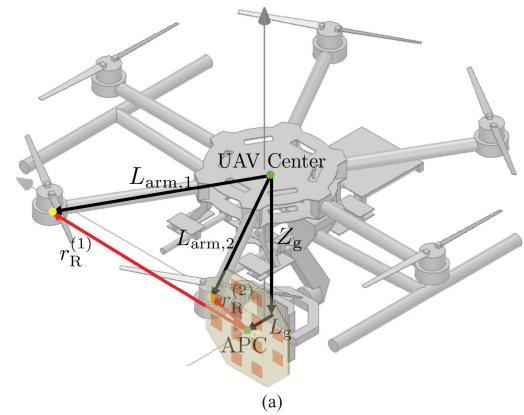


**FIGURE 2.** (a) Geometry for two radiating elements at the extremes of the arms of an hexacopter. (b) Antenna pattern for probe (co-polarization, solid; cross-polarization, dashed), and probe mounted on UAV (co-polarization, dash-dotted; cross-polarization, dotted).

## C. ERROR SOURCES
### 1) COUPLING

The scattering and reradiation of energy between the probe antenna and AUT may produce a measurable error in the region of the main lobe peak if the probe antenna produces a significant illumination taper along the test aperture. This effect is usually negligible in the side lobes [6]. The following derivation is valid for AUT and probe antennas of arbitrary radiation patterns. Assuming a polarization-matched case and reciprocity between AUT and probe antenna, when the load is not ideally matched, a fraction of the received signal will also be reradiated, resulting in a net combined effect of a backscattered signal due to scattering and reradiation that may be only a few decibels below the received signal. Following the procedure from [6] in a more general sense and noting that $P \propto E^2$, the effect of the coupling between the AUT and probe may be estimated as:

$$E_{\mathrm{C}}(\theta, \phi) = k_{\mathrm{s}} k_{\mathrm{r}} \frac{E_0}{r_{\mathrm{D}}^2} f^{\mathrm{AUT}}(\theta, \phi) f^{\mathrm{P}}(\theta, \phi) e^{-j2kr_{\mathrm{D}}}, \tag{21}$$

where $E_{\mathrm{C}}$ is the coupled illuminating field received at the AUT due to reradiation and $k_{\mathrm{s}}$, $k_{\mathrm{r}}$ are the coefficients of the back-scattered and retransmitted signals, respectively. Typical values of $k_{\mathrm{s}} = k_{\mathrm{r}} = 0.25$ as reported in [6] are used throughout the analyses. Then, the error contribution in the

measurement due to coupling can be estimated as

$$\Delta E_{\mathrm{C}} = 20 \log \left( 1 \pm \frac{E_{\mathrm{C}}}{E_{\mathrm{D}}} \right). \tag{22}$$

### 2) EXTRANEOUS REFLECTIONS

The coherent interference of an extraneous signal with the direct-path signal will produce a well-defined interference pattern at the AUT if the level of the composite reflected signals relative to the direct-path signal is significant [6]. For this work, it is assumed that a signal is being reflected off of the surface in front of the AUT; see Fig. 3 for a diagram.
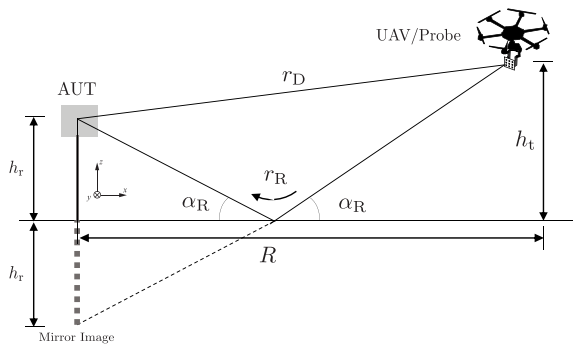


**FIGURE 3.** Generic measurement setup and geometry of the ground-reflected rays.

A simple ground reflection model is selected, and the signal is defined as:

$$E_{\mathrm{R}}(\theta, \phi) = \frac{E_0 \Gamma(\alpha_{\mathrm{R}})}{r_{\mathrm{R}}} f^{\mathrm{AUT}}(\theta, \phi - \alpha_{\mathrm{R}}) f^{\mathrm{P}}(\theta, \phi - \alpha_{\mathrm{R}}) e^{-jkr_{\mathrm{R}}}, \tag{23}$$

with [46]

$$\Gamma(x) = \frac{\sin x - R}{\sin x + R} \tag{24}$$

and

$$R = \begin{cases} \sqrt{\varepsilon_g - \cos^2 x}, & \text{for H-polarization,} \\ \dfrac{\sqrt{\varepsilon_g - \cos^2 x}}{\varepsilon_g}, & \text{for V-polarization,} \end{cases} \tag{25}$$

where $r_{\mathrm{R}}$ is the length of the ground-reflected ray, $\alpha_{\mathrm{R}}$ is the angle of reflection, and $\epsilon_g$ the permittivity of the ground. The co-polarized and cross-polarized components can be found following similar steps as previously shown. It is important to note that this angle of specular reflection can be different for the AUT and the probe depending on the relative height between the two and must be accounted for when extracting the correct value from the antenna patterns. The value of $\epsilon_g = 3 - j0$ is used here, as a low representative value for the permittivity of soil [47].

Furthermore, an approximation of the effects of a composite coherent extraneous signal is useful in evaluating the

potential error levels, regardless of the direction of arrival [6]. The relative measured error can be obtained as

$$\Delta E_{\mathrm{R}} = 20 \log \left( 1 \pm \frac{E_{\mathrm{R}}}{E_{\mathrm{D}}} \right), \tag{26}$$

for $E_{\mathrm{D}} > E_{\mathrm{R}}$, which can account for both in-phase and out-of-phase signals. In the unlikely event that $E_{\mathrm{D}} < E_{\mathrm{R}}$, the expression $\Delta E_{\mathrm{R}} = 20 \log(E_{\mathrm{R}}/E_{\mathrm{D}} \pm 1)$ is used instead.

### 3) POSITION AND ORIENTATION MISALIGNMENT

Measurement errors from a number of sources related to the alignment, i.e., position and orientation, of the AUT and probe antennas must be considered when determining the accuracy of the antenna range. For UAV-based measurements, these errors are related directly to the accuracy of the individual component, which have an impact on the position and orientation of the platform. Position and orientation drifts may occur due to the difference between their real value and the value that is measured, which is subject to inaccuracy of the instrument, environmental conditions (e.g., wind), and the flight controller control algorithm. Each instrument has its intrinsic errors (e.g., bias, drift, noise figure, etc.), which can be found in the datasheet, that affect the precision of the measurement of the radiation pattern.

In the simulation framework, $x$, $y$ and $z$ denote the real position of the UAV in a cartesian coordinate system with the origin at the AUT phase center analogous to the east-north-up (ENU) coordinate system, and $\Delta x$, $\Delta y$ and $\Delta z$ their uncertainties in the respective directions (which are predominantly affected by the GPS accuracy; the barometer accuracy affects the height measurement for the most part). The distances between the AUT and the center of the UAV are given by $r_{\mathrm{D}} = \sqrt{x^2 + y^2 + z^2}$ (real), and $r'_{\mathrm{D}} = \sqrt{(x + \Delta x)^2 + (y + \Delta y)^2 + (z + \Delta z)^2}$ (measured). Assuming there is no alignment error in orientation, the difference between real and measured positions would generate a difference in path loss of

$$\Delta L_{\mathrm{o}} = 20 \log \frac{r_{\mathrm{D}}}{r'_{\mathrm{D}}}. \tag{27}$$

In addition to an offset in position, the uncertainties may propagate to the relative orientation between the AUT and the UAV. The real and measured $\theta$ and $\phi$ angles may be obtained as: $\theta = \cos^{-1} \frac{z}{r}$, $\theta' = \cos^{-1} \frac{z + \Delta z}{r'}$, $\phi = \tan^{-1} \frac{y}{x}$, and $\phi' = \tan^{-1} \frac{y + \Delta y}{x + \Delta x}$. This effect produces a change in the amplitude and phase of the radiation pattern being measured, in the sense that the relative direction between the probe antenna and AUT is different from boresight. Assuming the AUT is stationary at the time step where the measurement with the UAV is taken, and that there is no position error, then

$$\Delta L_{\mathrm{o}} = 20 \log \frac{f^{\mathrm{P}}(\theta', \phi')}{f^{\mathrm{P}}(\theta, \phi)}, \tag{28}$$

represents the change in the radiation pattern due to the AUT and probe misalignment.

## D. TOTAL MEASURED SIGNAL

The total measured signal is obtained as the sum of the transmitted direct-path signal, and the effects of perturbations considered herein, which can be summarized as:

$$E_T = E_{D_{dB}} + \Delta E_R + \Delta E_C, \qquad (29)$$

from which the total error between the measured and real signals can then be computed. It is noted that, these effects are directly or indirectly related to the wave number $k$, and as such they scale accordingly with the operating frequency of the system.

## IV. ANALYSIS

In the previous sections, the methodology and models used herein have been be explained, in addition to how the errors are evaluated. Clearly, any variable that is dependent on the position and orientation of the AUT and/or probe will be potentially affected by vibrations, instabilities, and misalignment, which would produce variations in the measured signal. As such, the misalignment errors are generally coupled with the coupling and reflection errors, and it would be very difficult to create an error budget for every error source. Thus, the analysis here will focus mainly on position and orientation errors in the measurements.

Two cases are discussed and compared: the elevated range model (i.e., similar to hovering but with little to no perturbations in position and orientation), and the hovering UAV-based model. A brief discussion shall be presented on the overall aspects that are critical to each setup and how to mitigate potential error sources.

### A. CASE I: PROBE IN AN ELEVATED RANGE

In this scenario, the AUT is mounted on top of a structure with $h_r = 12.2$ m above the ground, and the probe is mounted on a pedestal separated by a distance of $R = 425$ m, at a height of $h_t = 40$ m above the ground, which attempts to replicate a test setup presented in [39]. With this configuration, the FF distance criterion is achieved with a factor $K = 2.66$, based on equation (1), and the phase curvature inductive coupling effects and can be safely disregarded. There is no significant longitudinal taper, and for the selected probe characteristics, the beamwidth is sufficiently larger than the angle subtended by the AUT at the probe, such that the mutual coupling and transversal taper effects are within the suggested design requirement limits. In other words, the beamwidth at the 0.25 dB level is $\theta_{0.25} = 3.4°$ for the probe antenna, and $\alpha_D = 0.54°$ in this scenario, such that the criterion $\theta_{0.25} > \alpha_D$ is met. However, with a wide beamwidth, ground reflections are of concern in this setup, since the ground reflection criterion is not met, i.e., FNBW/2 $> \alpha_{h_r}$, with $\alpha_{h_r} = 1.63°$ and FNBW/2 $= 30°$. In addition to the effect of reflections, variations in the position of the probe (e.g., due to load changes, deflections, wind), and variations in the orientation of the probe (e.g., due to vibration and accuracy of the positioner, and misalignment effects derived from variations in position) will also contribute to measurement errors.

The probe is assumed to be fixed atop the pedestal pointing directly towards the AUT, and the position errors are modeled independently for the three Cartesian axes $(x, y, z)$ as a zero-mean Gaussian distribution with their respective standard deviations $(\sigma_x, \sigma_y, \sigma_z)$. The parameters for the Gaussian error model have been determined through actual experiments in the field: with the UAV stationary at different locations higher than the ground to avoid GPS multipath issues, with the UAV hovering above some height off the ground in calm winds, and with the UAV hovering in relatively strong winds. A statistical analysis of the positioning in each case was produced, and the standard deviations were derived for the error models. Since the positioning error can be manually adjusted in the simulated framework, the error analysis becomes decoupled from the specific type of hardware being used; thus, virtually any hardware from different vendors can be tested. The values selected here represent the platform used in this study; the results for a GPS, and a DGPS device have been presented in [26]. The AUT is assumed to be fixed atop a robust tower, such that there are no errors in position (i.e., the AUT is not rotating), and the scan is performed electronically by means of beam steering from $-45$ to $45°$ in azimuth and at a fixed elevation of $0°$ relative to the AUT. The accuracy for typical indoor test range equipment, can be found in [6]. Here, an example is provided with $\sigma_x = \sigma_y = 1$ cm, and $\sigma_z = 3$ cm, corresponding to calm wind conditions and a relatively smooth terrain, such that there is no significant variability of the position in any direction. A number of samples ($M = 20$) are taken for each direction, similar to standard measurement techniques. Fig. 4 shows the simulated patterns with and without errors, averaged over 20 samples per direction in azimuth.

Both sets have been normalized with respect to the error-less pattern, and the reduction in directivity is apparent. Between the polarizations; however, the co-polarization bias is 0.02 dB, while the cross-polarization bias is in the order of 5 dB. This difference is explained by the fact that the ground-reflected signals can be adding either constructively or destructively depending on the difference of the direct-path and reflected-path lengths, which has different effects depending on the polarization. The higher cross-pol level remains below the required threshold at about $-55$ dB.

### B. CASE II: PROBE MOUNTED ON A UAV

A scenario similar to Case I is studied next, where the UAV is hovering about the height of the pedestal of the elevated range configuration. The main differences between the two cases are that the position errors are much higher due to the lower accuracy of the instruments (e.g. DGPS, IMU, and baroaltimeter) on the UAV, and the orientation errors due to gimbal inaccuracy. For the sake of simplicity, the orientation accuracy for the roll, pitch, and yaw axes of the UAV relative to the gimbal are not taken into account, though it is noted that the propagation of such errors would ultimately induce an error in the pointing direction of the gimbal. Previous benchmark testing on the equipment used in this study provides
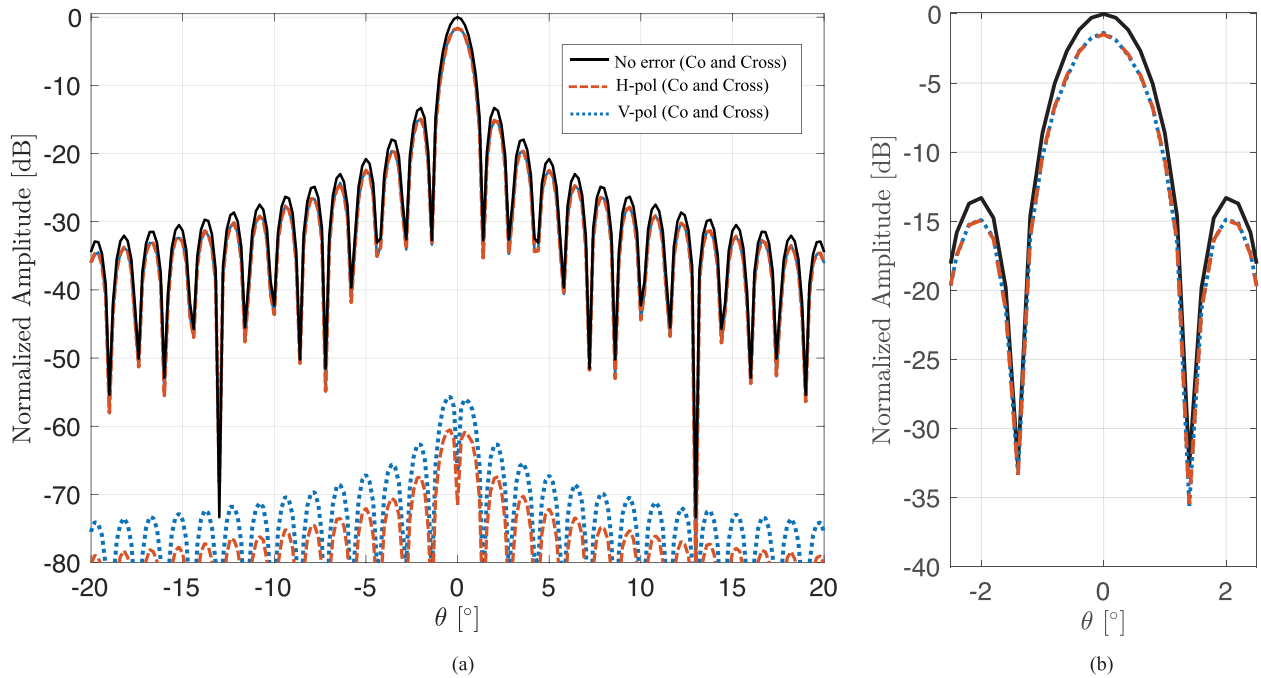
**FIGURE 4.** Case I: Probe in an elevated range. (a) Simulated measurements with (blue, red) and without (black) errors for H-polarized (blue) and V-polarized (red) antenna patterns, with top lines corresponding to co-polarization patterns, and bottom lines corresponding to cross-polarization patterns. (b) Zoomed-in plot.
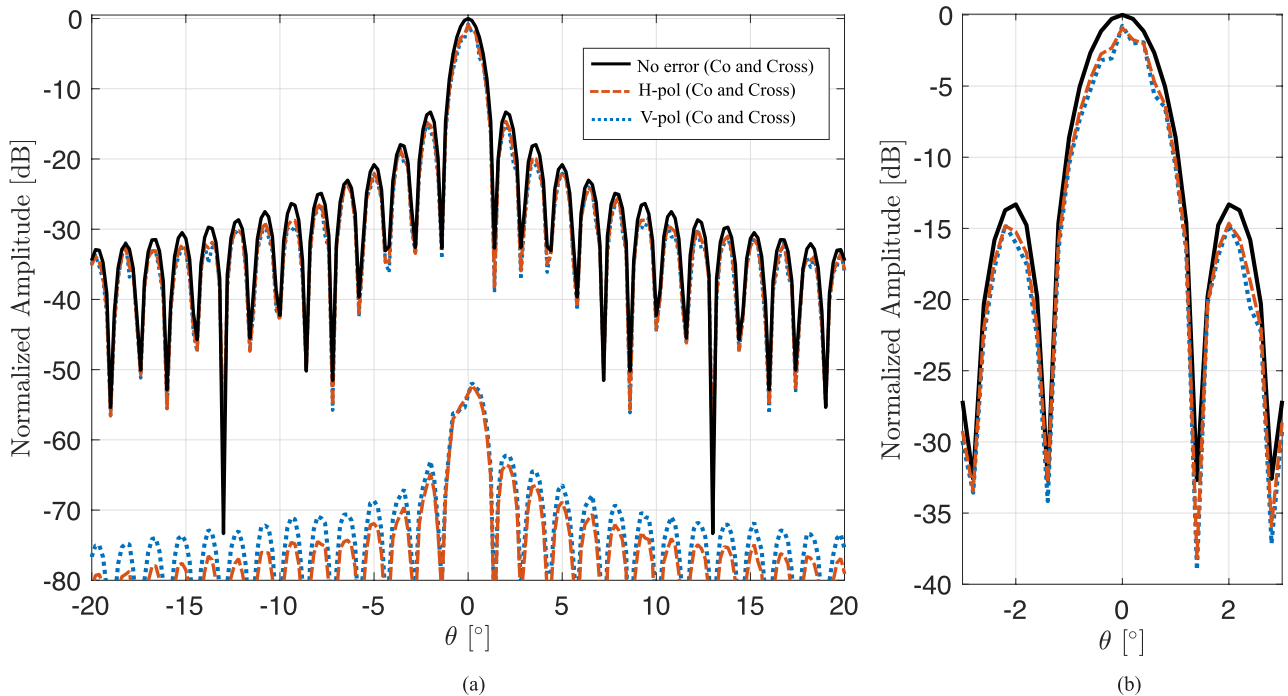


**FIGURE 5.** Case II: Probe mounted on a UAV. (a) Simulated UAV-based measurements with (blue, red) and without (black) errors for H-polarized (blue) and V-polarized (red) antenna patterns, with top lines corresponding to co-polarization patterns, and bottom lines corresponding to cross-polarization patterns. (b) Zoomed-in plot.

the expected accuracy for the UAV system under calm winds, with $\sigma_x = \sigma_y = 10\,\text{cm}$, $\sigma_z = 30\,\text{cm}$, and the azimuth and elevation accuracy $\sigma_\theta = \sigma_\phi = 0.02°$ per vendor specifications. The simulation is run with the AUT scanning electronically, while the probe mounted on the UAV is hovering at an altitude

of approximately 40 m above ground level, taking 20 samples for each direction in azimuth. The results are shown in Fig. 5.

Although subject to the random nature of the iterations in the simulation, the features that are evident are the asymmetry and the higher cross-pol level introduced by the
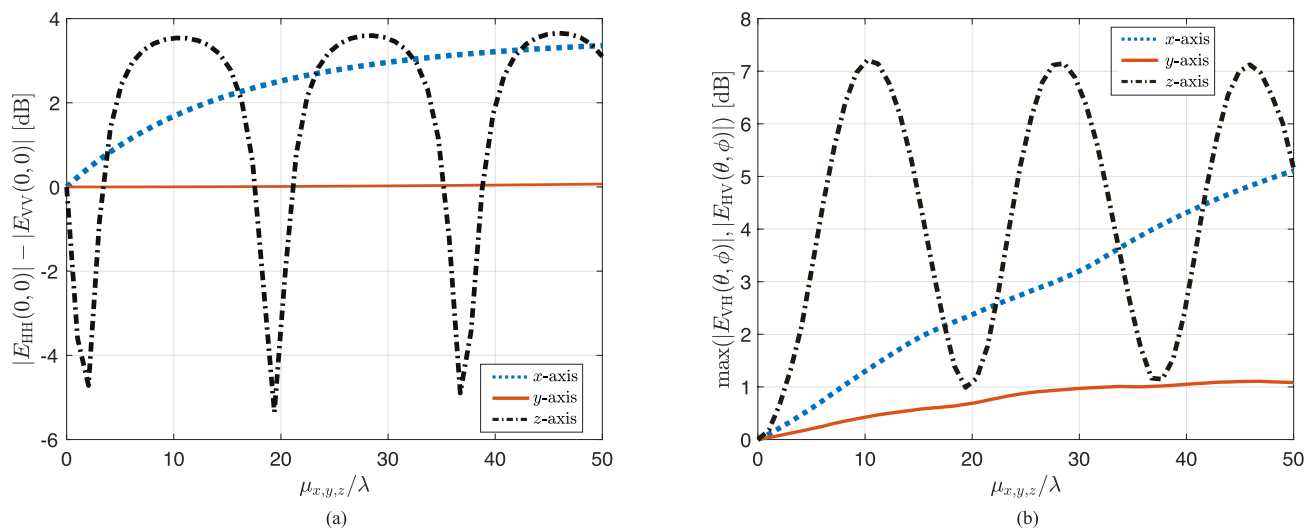
**FIGURE 6.** Normalized variations for the different directions in the *x*- (east), *y*- (north), and *z*- (north) axes as function of the bias in position for: (a) co-polarization mismatch levels, and (b) cross-polarization level increment.

UAV structure itself, and the higher variability in the measured patterns, still evident even for 20 averaged samples, due to higher position and orientation errors. Additionally, the null of the "real" cross-polarization pattern at boresight is obscured by signal contamination. In this particular case, the co-polarization bias is seen to increase to 0.15 dB, and the cross-polarization pattern level is approximately 3 dB higher than in the elevated range measurement. It is important to note that no probe correction techniques have been applied to these data sets, and as such, improvements on the estimates can be made but are out of the scope of this work. However, other works [8], [23], [26], [27] have dealt with mitigating the effects of reflection, diffraction, and scattering off the UAV.

### C. MISALIGNMENT ERROR ANALYSIS

In addition to analyzing the effect of flight precision with a UAV (represented herein as Gaussian models with a given mean and standard deviation), it is important to study the effect of inherent biases in positioning and targeting with the mobile system, i.e., when the mean is different from zero. Such biases may be introduced by means of gimbal drift, instrumentation biases, measurement noise, and probe misalignment, to name a few. The relative orientation between probe antenna mounted on the UAV's gimbal, and the AUT, can have a substantial effect in modifying the radiation pattern of the probe antenna, as was discussed in previous sections. As such, an estimation of the errors introduced by this misalignment is extremely important in attaining the desired accuracy and precision for the weather radar system requirements. While [43] has dealt with a similar problem, this approach attempts to tackle the problem considering variations both in azimuth and elevation for different gimbal orientations. It should be noted that this analysis corresponds to a 4 × 4 probe antenna, the AUT described previously, and for assumptions regarding coupling and extraneous signals

that were derived for the purpose of this work. However, such analyses may be extended to a large number of different scenarios, provided that the relevant parameters can be sufficiently estimated.

Fig. 6 shows the co-polarization pattern mismatch at boresight (i.e., the deviation between the H-polarized and V-polarized signals), and the normalized cross-polarization level variation for various displacements in the *x*-, *y*-, and *z*- axes as function of $\lambda$. The ordinates represent the increase or decrease in variable of interest, while the abscissa represents the position bias normalized by the wavelength. It can be seen that the *y*-axis position errors are the least affected, as expected, since the motion along this axis would be mostly transversal to the direction of propagation. In the direction of the *x*-axis, a longitudinal taper due to the path loss has a greater effect, while in the *z*-axis, though also a transversal motion, the ground reflections produce a ripple effect as explained in [6]. While the range of motion being analyzed is rather large (up to 50 $\lambda$ or 5 m), standard GPS modules can have uncertainties of a few meters. Moreover, this highlights the importance of having position accuracy and precision in the order of a few centimeters whenever possible such that these variations are kept to a minimum. Additionally, the altitude uncertainties are usually higher than those in the *x*- and *y*-axes, and the use of a lidar for altitude reading may aid in improving the antenna measurements.

Misalignment between the AUT and probe may also be a source of error as previously mentioned. For this, the biases of the signal for both co- and cross-polarization components is studied as a function of the gimbal elevation bias. Fig. 7 shows the co-polarization mismatch and the cross-polarization level variation as function of the bias in gimbal elevation angle. It is apparent that the cross-polarization signal is attenuated at lower elevation angles due to the fact that there are less reflections off the UAV structure. However, the actual values of the
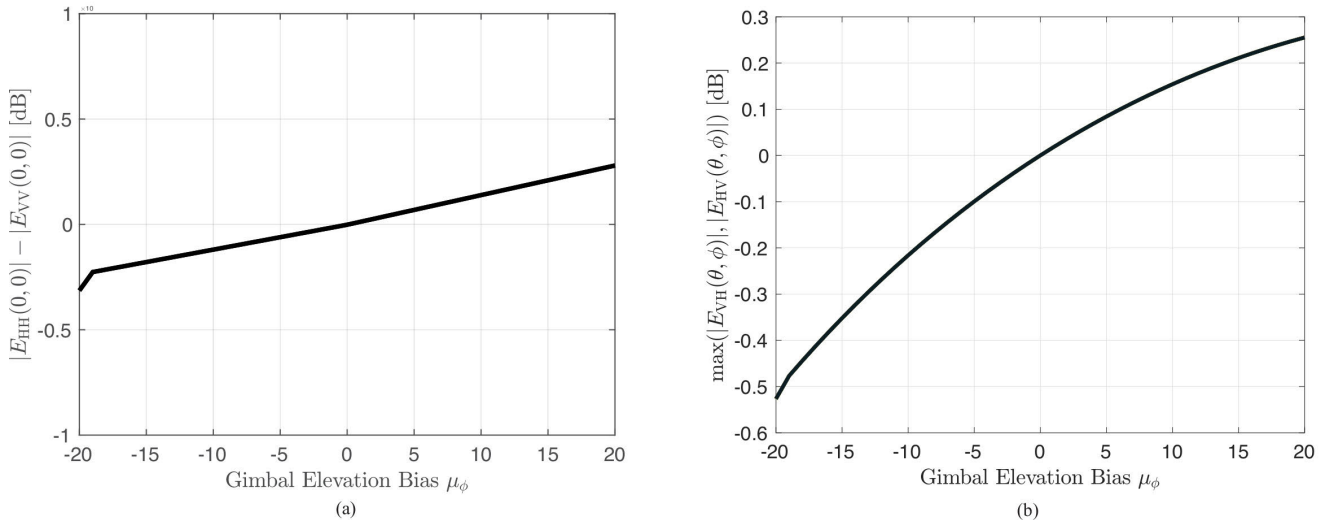
**FIGURE 7.** Normalized variations as function of the bias in gimbal elevation for: (a) co-polarization mismatch levels, and (b) cross-polarization level increment.
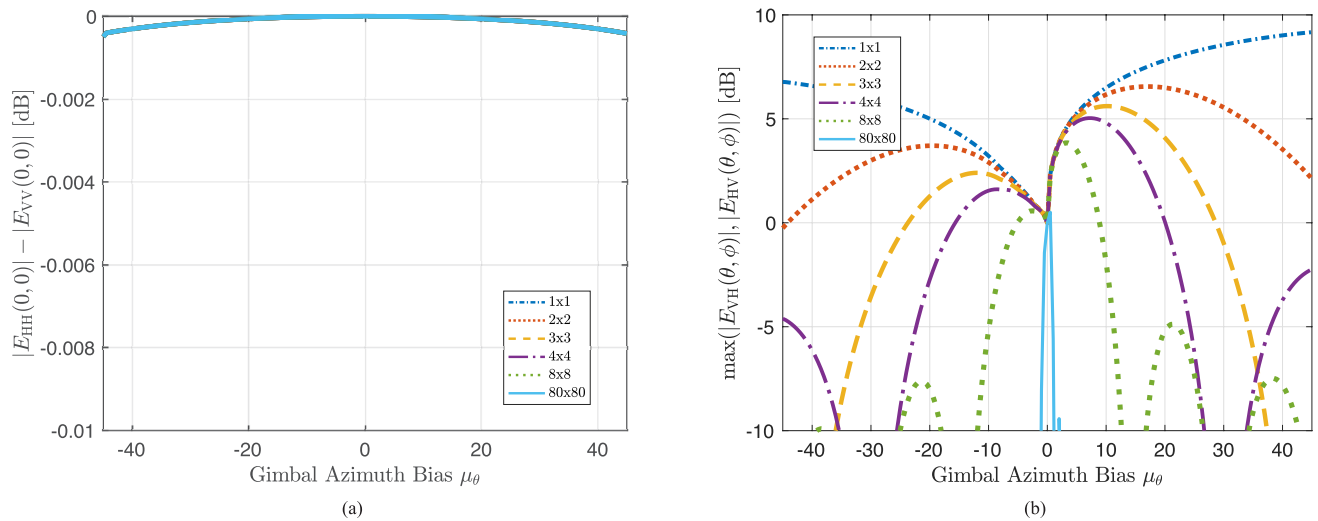


**FIGURE 8.** Normalized variations as function of the bias in gimbal azimuth, and for different probe array configurations of 1 × 1, 2 × 2, 3 × 3, 4 × 4, 8 × 8, and 80 × 80 elements, for: (a) co-polarization mismatch levels, and (b) cross-polarization level increment.

levels are dependent on the model being used, and one must be critical when interpreting results as they may be higher for different setups. Also note that the positioning accuracy must be sufficiently good, in addition to the gimbal accuracy, because misalignment is also affected by the relative position between the AUT and the UAV-probe system.

The biases in gimbal azimuth can also introduce measurement errors. Fig. 8 shows plots similar to Fig. 7, except that the abscissa is now the bias of the gimbal azimuth angles for different probe array antennas. The co-polarization components are seen to have a very small variation, suggesting that it is practically independent of the array antenna size. More importantly, it can be seen that the cross-polarization levels exhibit a relatively predictable behavior for arrays

with wider beamwidths and at small azimuthal biases (i.e., $|\mu_\theta| < 2°$) though in increasing nature, while for more directive beamwidths, it shows the opposite behavior–that is, the levels are lower but exhibit a pattern similar to that of the probe antenna's array factor. In general, this is desired because the cross-polarization levels are actually lower than that without azimuth bias; however, the main drawback here is that with increasing probe antenna size, it becomes harder to be physically feasible (UAV payload and size constraints). As such, it should be noted that larger probe antennas presented here are intended only for reference and not necessarily the "holy grail" for UAV-based antenna measurements for weather radars. Additionally, while the range of azimuth bias is set arbitrarily large (ideally, this measurement bias

should not be larger than a few degrees off boresight), this exercise illustrates the wide range of variation for the cross-polarization component of the probe antenna. It should be understood that the dominating effects for this variability are reflections off of extraneous sources and from the structure of the UAV itself.

### D. DISCUSSION

It is shown that for the fixed probe (case I), the co-polarization mismatch is in the order of 0.02 dB, while the cross-polarization bias is in the order of 5 dB above the nominal level; while for the mobile probe (case II), the co-polarization mismatch is 0.15 dB and the cross-polarization level is approximately 8 dB higher than expected. This is attributed to the errors in position, due to differences in the accuracy $(\sigma_x, \sigma_y, \sigma_z)$ between both cases. This suggests that as long as the positioning precision of the UAV is increased, the co- and cross-polarization requirements of 0.1 and $< -50$ dB, respectively, for polarimetric weather radars can be achieved. Additionally, it is desired that the gimbal operation mode allows targeting the AUT within an acceptable range, such that the biases introduced due to gimbal azimuth and elevation misalignment are minimal. In other words, the relative orientation between the probe antenna and the UAV frame should be known and used as an advantage. For example, the least amount of error introduced in the measurement both for the co-polarization mismatch and the cross-polarization levels is when the gimbal is aligned with the nose of the UAV frame; and if the orientation of the gimbal varies within $\pm 5°$ in either azimuth or elevation, then a co-polarization mismatch of $<0.1$ dB and a cross-polarization bias of $<5$ dB can be guaranteed.

Based on the results provided here and under the assumptions made for these particular cases, it is recommended to use a probe antenna with as narrow a beamwidth as possible while still being physically realizable, and to prioritize the altitude accuracy over the $x$-$y$ accuracy to keep the error levels at a minimum. Additionally, it must be understood that the variance of the measurements (caused mostly by variations about the mean position and orientation) may be reduced by taking more samples for averaging, which would introduce an error level similar to that of the UAV hovering about a nominal position. However, actual biases in the position and orientation are stronger sources of errors, as was shown. Also worth mentioning is the fact that a larger probe antenna will impact negatively on the payload and endurance of the UAV system, thus limiting the scanning strategy possible with a particular system. The larger the aperture of the AUT, the greater the FF distance, and the selection of a scanning strategy that maximizes the endurance (minimizes the time taken for a desired scan) becomes important.

### V. CONCLUSION

Recommendations for UAV-based antenna characterization have been presented with an analysis of the errors for particular cases, and a framework which allows the evaluation of errors due to position, orientation, and extraneous error sources has been developed. The results are analyzed for different case studies which can provide the error bounds and limitations for various characterization schemes.

By assuming a static source (i.e., minimal position variation), the errors for an elevated range have been evaluated, which yielded a co-polarization mismatch of approximately 0.02 dB, and a cross-polarization level of approximately $-55$ dB. A similar case study but for a UAV hovering about the same height as the pedestal for the elevated range case has been studied, which yielded a co-polarization mismatch of 0.15 dB and a cross-polarization level of approximately $-52$ dB, which suggests that a UAV-based antenna characterization method can be as effective as an elevated range, provided that the accuracy of the navigation and tracking system are sufficient. Also note that in neither case probe correction techniques have been applied, which would further improve the error levels. In a similar manner, the dependency of the position biases indicated that a bias in the altitude measurements can produce large variations in the error levels of the co- and cross-polarization patterns. The dependency with regards to the $x$-axis position bias, which relates to the longitudinal distance from the AUT, was also of significant according to the results. The transversal motion along the $y$-axis yielded the smallest errors. The gimbal azimuth bias has a strong effect on the cross-polarization levels, which can be mitigated by the use of more directive probes; however, the trade-off is that it impacts the payload and endurance of the UAV negatively, and thus, this factor must be considered when selecting the probe for a particular mission. In general, this azimuth bias should be kept to a minimum with gimbal subsystems that can provide better tracking accuracy, usually in the order of $\pm 0.02°$. The variation in the co-polarization mismatch due to gimbal azimuth bias is shown to be less affected by misalignment. Additionally, in a similar manner, gimbal elevation biases can have an effect of varying the co-polarization mismatch and the cross-polarization levels, which is shown to be attenuated as the gimbal points away from the direction of UAV reflections.

This suggests and supports the feasibility of such a system for antenna characterization and polarimetric calibration of antennas in the near future.

## REFERENCES

[1] T. D. Crum and R. L. Alberty, "The WSR-88D and the WSR-88D operational support facility," *Bull. Amer. Meteorol. Soc.*, vol. 74, no. 9, pp. 1669–1688, 1993.

[2] J. E. Stailey and K. D. Hondl, "Multifunction phased array radar for aircraft and weather surveillance," *Proc. IEEE*, vol. 104, no. 3, pp. 649–659, Mar. 2016.

[3] I. R. Ivic, "An approach to simulate the effects of antenna patterns on polarimetric variable estimates," *J. Atmos. Ocean. Technol.*, vol. 34, no. 9, pp. 1907–1934, Sep. 2017.

[4] C. Fulton, J. Salazar, D. Zrnic, D. Mirkovic, I. Ivic, and D. Doviak, "Polarimetrie phased array calibration for large-scale multi-mission radar applications," in *Proc. IEEE Radar Conf. (RadarConf)*, Apr. 2018, pp. 1272–1277.

[5] "IEEE standard test procedures for antennas," Inst. Elect. Electron. Eng. (IEEE), Princeton, NJ, USA, Tech. Rep., 1979, vol. 149, no. 1979.

[6] J. S. Hollis, T. Lyon, and L. Clayton, *Microwave Antenna Measurements*. San Jose, CA, USA: Scientific-Atlanta, 1970.

[7] C. A. Balanis, *Antenna Theory: Analysis and Design*. Hoboken, NJ, USA: Wiley-Interscience, 2005.

[8] S. T. P. Duthoit, "UAV-based *in situ* antenna characterization: Analysis and design requirements," M.S. thesis, 2018.

[9] J. Steele, "Measurement of antenna radiation patterns using a tethered balloon," *IEEE Trans. Antennas Propag.*, vol. 13, no. 1, pp. 179–180, Jan. 1965.

[10] J.-E. Lejerkrans and F. Enquist, "Field strength measurement and antenna radiation pattern plotting using heli-borne equipment," in *Proc. Int. Broadcast. Conv.*, Sep. 1988, pp. 137–142.

[11] R. Manton and K. Beeke, "HF antenna radiation patterns over real terrain," in *Proc. Int. Broadcast. Conv.*, Sep. 1988, pp. 143–147.

[12] G. Virone, A. M. Lingua, M. Piras, A. Cina, F. Perini, J. Monari, F. Paonessa, O. A. Peverini, G. Addamo, and R. Tascone, "Antenna pattern verification system based on a micro unmanned aerial vehicle (UAV)," *IEEE Antennas Wireless Propag. Lett.*, vol. 13, pp. 169–172, 2014.

[13] G. Virone, F. Paonessa, O. A. Peverini, G. Addamo, R. Orta, R. Tascone, A. Lingua, M. Piras, P. Bolli, G. Pupillo, and J. Monari, "Antenna pattern measurement with UAVs: Modeling of the test source," in *Proc. 10th Eur. Conf. Antennas Propag. (EuCAP)*, Apr. 2016, pp. 1–3.

[14] F. Paonessa, G. Virone, P. Bolli, G. Pupillo, J. Monari, F. Perini, A. Mattana, G. Naldi, M. Poloni, M. Schiaffino, A. M. Lingua, M. Piras, P. Dabove, I. Aicardi, G. Addamo, O. A. Peverini, R. Orta, and R. Tascone, "The UAV-based test source as an end-to-end verification tool for aperture arrays," in *Proc. Int. Conf. Electromagn. Adv. Appl. (ICEAA)*, Sep. 2016, pp. 886–889.

[15] F. Paonessa, G. Virone, E. Capello, G. Addamo, O. A. Peverini, R. Tascone, P. Bolli, G. Pupillo, J. Monari, M. Schiaffino, F. Perini, S. Rusticelli, A. M. Lingua, M. Piras, I. Aicardi, and P. Maschio, "VHF/UHF antenna pattern measurement with unmanned aerial vehicles," in *Proc. IEEE Metrol. Aerosp. (MetroAeroSpace)*, Jun. 2016, pp. 87–91.

[16] F. Paonessa, G. Virone, I. Aicardi, A. M. Lingua, M. Piras, P. Maschio, P. Bolli, G. Addamo, O. A. Peverini, R. Orta, and R. Tascone, "Recent results in antenna pattern measurement with UAVs," in *Proc. Int. Conf. Electromagn. Adv. Appl. (ICEAA)*, Sep. 2015, pp. 720–721.

[17] G. Virone, F. Paonessa, E. Capello, O. A. Peverini, G. Addamo, R. Tascone, R. Orta, M. Orefice, A. Lingua, M. Piras, I. Aicardi, P. Bolli, J. Monari, F. Perini, G. Pupillo, and M. Schiaffino, "UAV-based antenna and field measurements," in *Proc. IEEE Conf. Antenna Meas. Appl. (CAMA)*, Oct. 2016, pp. 1–3.

[18] G. Virone, F. Paonessa, O. A. Peverini, G. Addamo, R. Orta, R. Tascone, and P. Bolli, "Antenna pattern measurements with a flying far-field source (hexacopter)," in *Proc. IEEE Conf. Antenna Meas. Appl. (CAMA)*, Nov. 2014, pp. 1–2.

[19] G. Virone, F. Paonessa, A. Tibaldi, Z. Farooqui, G. Addamo, O. A. Peverini, R. Tascone, P. Bolli, A. Mattana, J. Monari, G. Naldi, F. Perini, G. Pupillo, M. Schiaffino, A. M. Lingua, M. Piras, P. Maschio, I. Aicardi, I. H. Bendea, and A. Cina, "UAV-based radiation pattern verification for a small low-frequency array," in *Proc. IEEE Antennas Propag. Soc. Int. Symp. (APSURSI)*, Jul. 2014, pp. 995–996.

[20] F. Paonessa, G. Virone, G. Addamo, O. A. Peverini, R. Tascone, E. D. L. Acedo, E. Colin-Beltran, N. Razavi-Ghods, P. Bolli, G. Pupillo, G. Naldi, J. Monari, A. M. Lingua, M. Piras, I. Aicardi, and P. Maschio, "UAV-based pattern measurement of the SKALA," in *Proc. IEEE Int. Symp. Antennas Propag. USNC/URSI Nat. Radio Sci. Meeting*, Jul. 2015, pp. 1372–1373.

[21] F. Üstuner, E. Aydemir, E. Güleç, M. Ilarslan, M. Celebi, and E. Demirel, "Antenna radiation pattern measurement using an unmanned aerial vehicle (UAV)," in *Proc. 31st URSI Gen. Assem. Sci. Symp. (URSI GASS)*, Aug. 2014, pp. 1–4.

[22] A. M. Picar, C. Marque, M. Anciaux, H. Lamy, and S. Ranvier, "Antenna pattern calibration of radio telescopes using an UAV-based device," in *Proc. Int. Conf. Electromagn. Adv. Appl. (ICEAA)*, Sep. 2015, pp. 981–984.

[23] S. Duthoit, J. L. Salazar, W. Doyle, A. Segales, B. Wolf, C. Fulton, and P. Chilson, "A new approach for *in-situ* antenna characterization, radome inspection and radar calibration, using an unmanned aircraft system (UAS)," in *Proc. IEEE Radar Conf. (RadarConf)*, May 2017, pp. 0669–0674.

[24] M. García-Fernández, Y. A. López, A. Arboleya, B. González-Valdés, Y. Rodríguez-Vaqueiro, M. E. D. C. Gómez, and F. L.-H. Andrés, "Antenna diagnostics and characterization using unmanned aerial vehicles," *IEEE Access*, vol. 5, p. 23 563–23 575, 2017.

[25] G. Pupillo, G. Naldi, G. Bianchi, A. Mattana, J. Monari, F. Perini, M. Poloni, M. Schiaffino, P. Bolli, A. Lingua, and I. Aicardi, "Medicina array demonstrator: Calibration and radiation pattern characterization using a UAV-mounted radio-frequency source," *Exp. Astron.*, vol. 39, no. 2, pp. 405–421, Jun. 2015.

[26] J. L. Salazar, A. Umeyama, S. Duthoit, and C. Fulton, "UAS-based antenna pattern measurements and radar characterization," in *Proc. IEEE Conf. Antenna Meas. Appl. (CAMA)*, Sep. 2018, pp. 1–4.

[27] A. Y. Umeyama, J. L. Salazar-Cerreno, B. M. Wolf, and C. J. Fulton, "Recent development in UAV-based antenna pattern characterization for weather radars," in *Proc. IEEE Conf. Antenna Meas. Appl. (CAMA)*, Oct. 2019, pp. 199–202.

[28] J. Yin, P. Hoogeboom, C. Unal, H. Russchenberg, F. van der Zwan, and E. Oudejans, "UAV-aided weather radar calibration," *IEEE Trans. Geosci. Remote Sens.*, vol. 57, no. 12, pp. 10362–10375, Dec. 2019.

[29] T. Fritzel, H. Steiner, J. Habersack, H. Schippers, and J. Ferrante, "Antenna pattern measurements of full-size air vehicles with an airborne near-field test facility (ANTF)," in *Proc. Eur. Test Telemetry Conf. (ETTC)*, 2005, pp. 1–6.

[30] L. Van Hoorebeeck, J. Cavillot, H. Bui-Van, F. Glineur, C. Craeye, and E. D. L. Acedo, "Near-field calibration of SKA-low stations using unmanned aerial vehicles," in *Proc. 13th Eur. Conf. Antennas Propag. (EuCAP)*, Mar./Apr. 2019, pp. 1–5.

[31] T. Fritzel, R. Strauss, H.-J. Steiner, C. Eisner, and T. Eibert, "Introduction into an UAV-based near-field system for *in-situ* and large-scale antenna measurements," in *Proc. IEEE Conf. Antenna Meas. Appl. (CAMA)*, Oct. 2016, pp. 1–3.

[32] M. G. Fernández, Y. Á. López, and F. Las-Heras, "Dual-probe near-field phaseless antenna measurement system on board a UAV," *Sensors*, vol. 19, no. 21, p. 4663, Oct. 2019.

[33] L. Ciorba, G. Virone, F. Paonessa, S. Matteoli, P. Bolli, E. D. L. Acedo, N. R. Ghods, J. Abraham, E. C. Beltrán, K. Z. Adami, A. Magro, O. A. Peverini, G. Addamo, G. Giordanengo, M. Righero, and G. Vecchi, "Near-field phase reconstruction for UAV-based antenna measurements," in *Proc. 13th Eur. Conf. Antennas Propag. (EuCAP)*, Mar./Apr. 2019, pp. 1–4.

[34] P. Bolli, G. Pupillo, F. Paonessa, G. Virone, S. J. Wijnholds, and A. M. Lingua, "Near-field experimental verification of the EM models for the LOFAR radio telescope," *IEEE Antennas Wireless Propag. Lett.*, vol. 17, no. 4, pp. 613–616, Apr. 2018.

[35] C. C. Cutler, A. P. King, and W. E. Kock, "Microwave antenna measurements," *Proc. IRE*, vol. 35, no. 12, pp. 1462–1471, Dec. 1947.

[36] F. Paonessa, G. Virone, P. Bolli, and A. M. Lingua, "UAV-based antenna measurements: Scan strategies," in *Proc. 11th Eur. Conf. Antennas Propag. (EUCAP)*, Mar. 2017, pp. 1303–1305.

[37] R. J. Mailloux, *Phased Array Antenna Handbook*. Norwood, MA, USA: Artech House, 2017.

[38] V. Chandrasekar and R. J. Keeler, "Antenna pattern analysis and measurements for multiparameter radars," *J. Atmos. Ocean. Technol.*, vol. 10, no. 5, pp. 674–683, Oct. 1993.

[39] D. J. Wasielewski, I. R. Ivic, and J. R. Mendoza, "Calibration of a dual-polarization planar phased-array radar using a far-field tower," in *Proc. Amer. Meteorol. Soc. Annu. Meeting*, 2019, p. 1.

[40] H. T. Friis, "A note on a simple transmission formula," *Proc. IRE*, vol. 34, no. 5, pp. 254–256, May 1946.

[41] Y. Wu and W. Huang, "Studies and analysis on unintentional electromagnetic radiation of UAV," in *Proc. IEEE 6th Int. Symp. Microw., Antenna, Propag., EMC Technol. (MAPE)*, Oct. 2015, pp. 479–482.

[42] A. Rizwan, D. Biswas, and V. Ramachandra, "Impact of UAV structure on antenna radiation patterns at different frequencies," in *Proc. IEEE Int. Conf. Antenna Innov. Mod. Technol. Ground, Aircr. Satell. Appl. (iAIM)*, Nov. 2017, pp. 1–5.

[43] F. Paonessa, G. Virone, A. M. Lingua, M. Piras, I. Aicardi, P. Maschio, O. A. Peverini, G. Addamo, R. Orta, R. Tascone, and P. Bolli, "Effect of the UAV orientation in antenna pattern measurements," in *Proc. 9th Eur. Conf. Antennas Propag. (EuCAP)*, Apr. 2015, pp. 1–2.

[44] E. C. Ngai, A. J. Fenn, A. K. Eapen, and E. F. Newman, "Radiation characteristics of small antennas on small UAV platforms," in *Proc. IEEE Antennas Propag. Soc. Symp.*, vol. 1, Jun. 2004, pp. 173–176.

[45] A. V. Khristenko, M. O. Konovalenko, M. E. Rovkin, V. A. Khlusov, A. V. Marchenko, A. A. Sutulin, and N. D. Malyutin, "Magnitude and spectrum of electromagnetic wave scattered by small quadcopter in *X*-band," *IEEE Trans. Antennas Propag.*, vol. 66, no. 4, pp. 1977–1984, Apr. 2018.

[46] W. C. Jakes and D. C. Cox, *Microwave Mobile Communications*. Hoboken, NJ, USA: Wiley-IEEE Press, 1994.

[47] J. Cihlar and F. T. Ulaby, "Dielectric properties of soils as a function of moisture content," Tech. Rep., 1974.

**JORGE L. SALAZAR-CERRENO** (Senior Member, IEEE) received the B.S. degree in ECE from University Antenor Orrego, Trujillo, Peru, the M.S. degree in ECE from the University of Puerto Rico, Mayagüez (UPRM), and the Ph.D. degree in ECE from the University of Massachusetts, Amherst, in 2011. At NCAR, he worked with the Earth Observing Laboratory (EOL) Division developing airborne technology for two-dimensional, electronically scanned, dual-pol phased array radars for atmospheric research. He joined the Advanced Radar Research Center (ARRC), The University of Oklahoma, as a Research Scientist, in July 2014. He was an Assistant Professor with the School of Electrical and Computer Engineering, in August 2015. His research interests include high-performance, broadband antennas for dual-polarized phased array radar applications, array antenna architecture for reconfigurable radar systems, APAA, Tx/Rx modules, radome EM modeling, millimeter-wave antennas, and development of low-cost dual-polarized active phased array antennas (APAA). He is a Senior Member of the IEEE Antennas and Propagation Society (AP-S). He received the Prestigious National Center for Atmospheric Research (NCAR) Advanced Study Program (ASP) Postdoctoral Fellowship and the Prestigious William H. Barkow Presidential Professorship from The University of Oklahoma for meeting the highest standards of excellence in scholarship and teaching, in 2019.

**CALEB J. FULTON** (Senior Member, IEEE) received the B.S. and Ph.D. degrees in electrical and computer engineering from Purdue University, West Lafayette, IN, USA, in 2006 and 2011, respectively. He is currently an Assistant Professor of electrical and computer engineering with the Advanced Radar Research Center, The University of Oklahoma, Norman, OK, USA. He is also involved in a number of digital phased-array research and development efforts for a variety of applications. His current research interests include antenna design, digital phased-array calibration and compensation for transceiver errors, calibration for high-quality polarimetric radar measurements, integration of low-complexity transceivers and high-power GaN devices, and advanced digital beamforming design considerations. He received the Purdue University Eaton Alumni Award for design excellence for his work on the Army Digital Array Radar Project, in 2009, the Meritorious Paper Award for a summary of these efforts from the 2010 Government Microcircuit Applications and Critical Technologies Conference, and the 2015 DARPA Young Faculty Award for his ongoing digital phased-array research.

**ARTURO YOSHIYUKI UMEYAMA** (Member, IEEE) received the B.S. degree in mechatronics engineering from the National University of Asunción, Asunción, Paraguay, in 2012, and the M.S. degree in electrical and computer engineering from The University of Oklahoma, Norman, OK, USA, in 2016, where he is currently pursuing the Ph.D. degree in electrical and computer engineering.

He is also a Graduate Research Assistant with the Advanced Radar Research Center, The University of Oklahoma. His research interests include advanced signal processing for weather radars, spectral analysis, and numerical radar simulation.

• • •